Appl Nanosci (2014) 4:839–847
DOI 10.1007/s13204-013-0264-3

ORIGINAL ARTICLE

Investigation of the optical property and photocatalytic activity of mixed phase nanocrystalline titania

Susmita Paul · Amarjyoti Choudhury

Received: 4 June 2013 / Accepted: 15 August 2013 / Published online: 4 September 2013

Abstract Mixed phase nanocrystalline titania are prepared by simple sol–gel method. The physico-chemical characteristics of the prepared nanoparticles are studied with X-ray diffraction, high-resolution transmission electron microscopy, RAMAN, BET, UV–Vis, steady state and time resolved photoluminescence. X-ray diffraction and Raman spectra clearly demarcate the anatase and rutile phase as both the phases give different diffraction patterns and Raman peaks. A comparison in the band gap indicates that pure anatase and rutile phase have band gap in the UV region, whereas a mixture of these phases has lower band gap and corresponds to the visible region. Steady state and time resolved photoluminescence are employed to understand the emissivity and carrier lifetime. The photocatalytic activity is evaluated by monitoring the degradation of phenol under visible light illumination. Due to the synergistic effect of mixed anatase and rutile phases, mixed phase nanocrystalline titania exhibit superior photocatalytic activity.

Keywords Mixed phase · Band gap · Carrier lifetime · Photocatalysis

Introduction

Titanium oxide (TiO_2) is one of the most important semiconductor oxides. Since the initial report by Fujishima and Honda (1972) on the photolysis of water by TiO_2, intense interests in the properties of nanocrystalline TiO_2 have been generated due to their promising applications in photocatalysis (Paul et al. 2013) and photoelectrochemical (Shin et al. 2013) energy conversion. TiO_2 belongs to the family of transition metal oxides. Four commonly known polymorphs of TiO_2: anatase, brookite, rutile, and TiO_2 (B) monoclinic exist in nature. Besides these two additional high pressure forms, TiO_2 (II) with a PbO_2 structure and TiO_2 (H) with a hollandite polymorphs are also known. From the catalytic viewpoint, anatase and rutile are the most important phase. The brookite phase is the rarest of the natural TiO_2 polymorphs and is the most difficult phase to prepare in the laboratory (Gupta and Tripathi 2011).

Anatase TiO_2 has a band gap of 3.2 eV (385 nm), while the rutile phase has a smaller band gap of 3.0 eV (410 nm). It is generally accepted that anatase TiO_2 is a better photocatalytic candidate compared to rutile TiO_2, but recently the anatase–rutile mixture is found to have a magical effect on the charge transfer process (Knorr.et.al 2008). The presence of rutile phase extends the photoactive response to the visible region, harvesting more light, and stabilization of charge separation by electron transfer from rutile to anatase trapping sites slows down the recombination (Hurum et al. 2003), thereby improving the photocatalytic activity.

Although there are several methods to prepare nanocrystalline titania but the sol–gel method represents several advantages over other methods (Zhou et al. 2006). As the method is carried out in solution, tailoring of certain desired structural characteristics such as compositional homogeneity, grain size, particle morphology, and porosity is possible with this method. The process finds wide applications in the development of new materials for catalysis (Oye et al. 2006), photochromic applications (Volkan et al. 2005), chemical sensors (Qui et al. 2011), and also in a diverge range of scientific and engineering

S. Paul · A. Choudhury (✉)
Department of Physics, Tezpur University,
Napaam 784028, India
e-mail: ajc@tezu.ernet.in

fields such as ceramic industry (Marinel et al. 2013), electronic industry (Lin 2013).

In the present investigation, nanocrystalline titania are prepared by simple sol–gel method. The phase transformation rearranges the bonding arrangement of TiO_2 and introduces many defects in the mixed phase sample. X-ray diffraction, TEM, Raman spectroscopy have been investigated to clearly distinguish the basic anatase and rutile phase, their sizes and the defects present. A detailed analysis on the optical properties of the reduced anatase, anatase–rutile mixed phase and of rutile phase are reported. Due to the synergistic effect of mixed anatase and rutile phases, an enhanced photocatalytic performance is noticed in the mixed phase titania.

Experimental methods

Material synthesis

The reagents used for the synthesis were titanium isopropoxide (TTIP, purity 97 %) and isopropanol (99 %). The synthesis was started by adding 15 ml of isopropanol to 5 ml titanium isopropoxide solution. The solution was allowed to stir for about 15 min and then 1 ml of water was added to initiate the hydrolysis process. The solution became turbid and the stirring was continued until gel formation (Dutta et al. 2009). The transformation from initial sol to gel took about 6–7 h. The gel was left for aging for about 12 h. This was followed by centrifugation with ethanol and water for 5 times. The centrifuged product was dried in an oven at 80 °C. Finally, the dried product was annealed at 450, 650, 850 °C for 3 h and the samples were labeled as T45, T65, T85, respectively.

Characterization details

The structure of all the samples is determined using Rigaku Miniflex CD 10041 XRD unit with copper target and $\lambda = 1.54$ Å at a scanning rate of 1°/min and in the scanning range of 10°–80°. High-resolution transmission electron microscopic images for morphology and particle size determination are observed with JEM-2100, 200 kV JEOL. Raman spectra of the samples are acquired with Reinshaw inVia spectrometer. The 514.5-nm emission of argon-ion laser is used as the excitation source. Surface area and pore size distribution of all the samples are studied with the help of a quantachrome instrument. Diffuse reflectance spectra (DRS) of the samples are taken with Shimadzu-2450 UV–Vis spectrometer. The photoluminescence (PL) measurements at room temperature are recorded with PERKIN ELMER LS 55 fluorescence spectroscopy. Time resolved photoluminescence spectra (TRPL) are recorded on an IBH Horiba-Yvon TCSPC using 340 nm Nano-LED (FWHM = 750 ps) and 375 nm nano-LED (FWHM = 300 ps) as excitation source for the samples with a time scale of 0.007 ns/channel.

Photocatalytic activity

Photocatalytic activity of the prepared TiO_2 nanoparticles was studied by examining the degradation of aqueous solution of phenol. For visible light irradiation, a 25-W white lamp was used. In order to carry out the process, 50 mg of the photocatalyst was mixed with 50 ml water in a 100-ml beaker. To this mixture, 5 mg of phenol was added and the solution was stirred for about half an hour in dark to obtain the absorption–desorption equilibrium (Choudhury et al. 2011). The catalyst loaded phenol solution was then placed at a distance of 6 cm and irradiated for 20, 40, 60 and 80 min. After completion of the irradiation process, the samples were centrifuged at 10,000 rpm to make it free from any catalyst. 5 ml of the aliquot was taken to measure the absorbance. The degradation efficiency is calculated using the following equation:

$$\%D = \left(\frac{A_O - A_t}{A_O}\right) \times 100 \quad (1)$$

where A_O is the initial absorbance and A_t is the absorbance after time t.

Results and discussions

Structural and morphological study

The XRD patterns are depicted in Fig. 1. The XRD pattern of the as-prepared powders shows the presence of brookite phase at 36° (JCPDS-761934). This phase is usually formed at low temperatures and gets disappeared at high annealing temperatures (So et al. 2001). On careful study of the phase transition of the samples, it is found that T45 resulted in pure anatase phase. The phase transition began at 650 °C and complete transformation to rutile phase occurred at 850 °C, in agreement with earlier results (Song et al. 2010; Li et al. 2008). The peaks in the spectra are in agreement with the JCPDS file nos. 782486 and 894202 of tetragonal systems for pure anatase and rutile phase, respectively. The average crystallite size of each sample (Table 1) is obtained taking the (101) peak for anatase, (110) for rutile and both (101), (110) for mixed phase using Scherer's formula:

$$d = \frac{0.9\lambda}{\beta \cos\theta} \quad (2)$$

Here d is the crystallite size, λ the wavelength of the X-ray (Cu $K_\alpha = 1.54$ Å), β the full width at half maximum, and θ

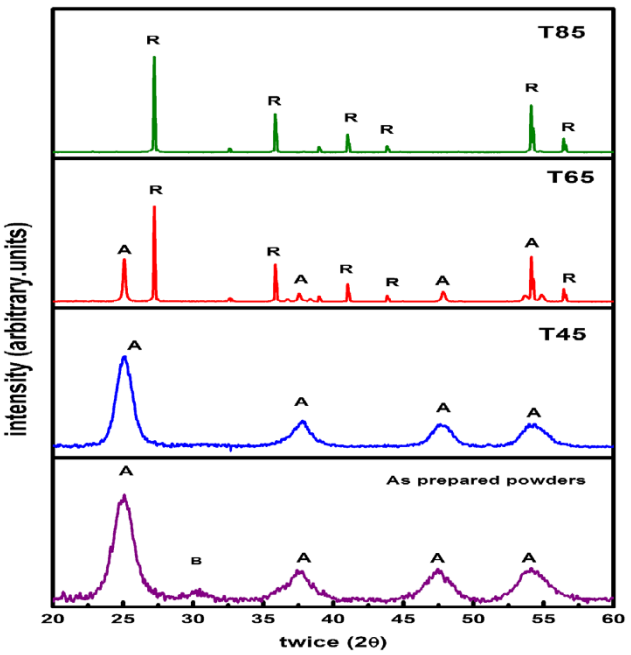

Fig. 1 X-ray diffraction pattern of all the samples

Table 1 Crystallite size, phase composition, band gap, Urbach energy details of the samples calcined at different temperatures

SI. no.	Calcination temp (°C)	Crystallite size (nm)		Fraction (%)		Band gap (eV)	Urbach energy (meV)
		Anatase	Rutile	Anatase	Rutile		
1.	450 (T45)	10	0	100	0	3.25	260
2.	650 (T65)	36	67	63.6	35.4	2.82	475
3.	850 (T85)	–	70	0	100	3.08	343

is the diffraction angle. The crystallite size is calculated to be in the nanoscale and a steady increase in size is noticed with the increase in annealing temperatures. Each of the anatase and rutile mass fractions of the samples is calculated using Spurr's formula (Spurr and Myers 1957):

$$f_a = \frac{1}{1 + 1.26\frac{I_a}{I_r}} \quad (3)$$

$$f_r = (1 - f_a) \quad (4)$$

where f_a and f_r are the anatase and rutile fractions, and I_a and I_r are the integrated intensities of the most intense anatase (101) and rutile (110) peak, respectively. The parameters calculated using Eqs. (3) and (4) are depicted in Table 1.

Figure 2a and b shows the TEM images of T45 and T65, respectively. The average particle size is small in case of pure anatase nanoparticles and increases with its transformation to mixed phase and then to pure rutile phase. For T45, the particle size distribution is within the range of ~16 nm, while for T65 it is 30–65 nm (Fig. 2b) and for T85 (Fig. 2c) the range is 126–230 nm. It is worth mentioning that we have obtained differences in the size calculated from XRD and TEM. The magnitude of the crystallite and particle size agrees well only for the case of stable, monodisperse, single crystals and hard spheres, and any deviation from this criteria leads to variation in measured sizes (Baalousha et al. 2012).

Raman spectroscopy is further employed in the characterization of crystalline structure of TiO_2 samples. Figure 3 shows the Raman spectra of all the samples. According to the group factor analysis, anatase has six active Raman modes at $(A_{1g} + 2B_{1g} + 3E_g)$ (Zhang et al. 2000), while for rutile TiO_2 group factor analysis gives four Raman active modes $(A_{1g} + B_{1g} + B_{2g} + E_g)$ (Aita 2007; Orendorz et al. 2007; Mazza et al. 2007). In our study in T45, a strong E_g peak appears at 144 cm^{-1} followed by the appearance of low intense peaks at 197 (E_g), 399 (B_{1g}), 513 $(A_{1g} + B_{1g})$ and 641 cm^{-1} (E_g). All these peaks correspond to the pure anatase phase. For T65 sample, E_g peak of anatase remains at 144 cm^{-1}, while additional peaks corresponding to the rutile phase appear at 236, 448, 613 cm^{-1} (Narksitipan and Thongtem 2012). In T85, all the Raman peaks identical to rutile TiO_2 predominate.

For a perfect crystal, the phonon contribution comes from the center of the Brilliouin zone satisfying the phonon momentum selection rule, $q \approx 0$ (Zhang et al. 2000). In semiconductor nanoparticles, the phonon selection rule breaks and the phonon momentum distribution increases. The phonon scattering thus involves phonon contribution from the entire Brillouin zone (Brojcin et al. 2005, Mo and Ching 1995). For nanoparticles of diameter (d), the intensity for first-order Raman scattering is given by:

$$I(\omega) = \frac{C0, k^2}{[\omega - \omega(k)]^2 + (\frac{\Gamma_o}{2})^2} d^3q \quad (5)$$

where $w(k)$ is the phonon dispersion curve, Γ_o the natural full line width and C $(0, k)$ is the fourier co-efficient of the phonon confinement function and is often in use as

$$|C(0,k)|^2 = \left(-k^2d^2/16\Pi^2\right) \quad (6)$$

where d is the average size of the nanocrystal. The changes in the Raman peaks are a result of this integration in Eq. (5) due to changes in grain size (Sharma et al. 2011).

In our study compared to T45, the E_g mode of T65 is slightly red shifted and the FWHM decreases. The phonon confinement model predicts that with the increase in crystallite size, the E_g peak is shifted to lower wave numbers and its FWHM and band intensity decrease (Orazen 2007).

Presence of oxygen defects also affects the Raman line, shape and position. The Raman spectra involve vibration of the oxygen atoms only (Georgescu et al. 2012). As the

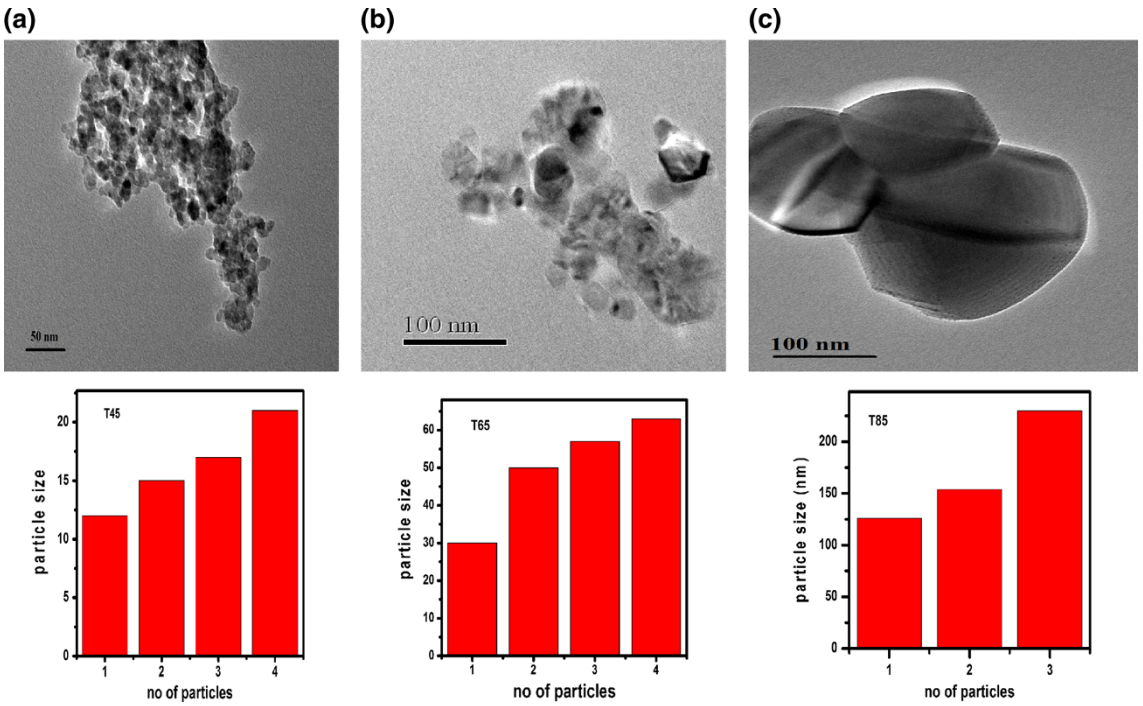

Fig. 2 TEM images of **a** T45, **b**T65, **c** T85

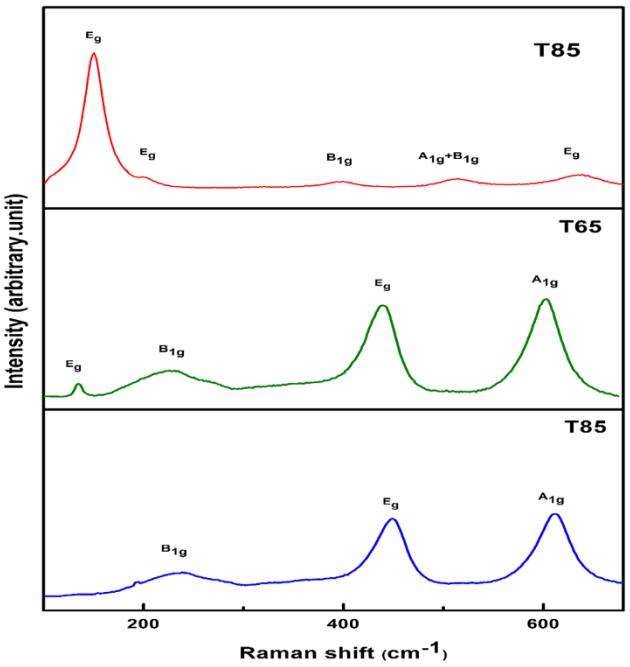

Fig. 3 Raman spectra of T45, T65, T85

temperature treatment changes the local co-ordination of oxygen atoms surrounding Ti^{4+}, switching from anatase to rutile phase involves the re-arrangement of TiO_6 octahedra that affects the Raman lines. We have calculated the phonon lifetime via the energy–time uncertainty relation $1/\tau = \Delta E/h = 1/2\ \pi c\Gamma$ (Mali et al. 2011), where ΔE is the uncertainty in energy, h is the Planck's constant and Γ is the FWHM of the Raman peaks in cm^{-1}. For T45 and T65, the phonon lifetime using the E_g mode is calculated to be 0.22 and 0.57 ps, respectively, while taking the A_{1g} mode for T65 and T85, the lifetime corresponds to 0.10 and 0.13 ps, respectively. The increased lifetime for T65 is attributed to the generation of increased defects due to the anatase–rutile contacts. In T85, an increase in crystal size adds to the increased phonon distribution further increasing the phonon lifetime (Wang et al. 2008).

Figure 4 shows the typical nitrogen adsorption isotherm. From the analysis, it is observed that the surface area and the pore size distribution determined from the BJH analysis exhibit a decrease with the increase in annealing temperatures (Table 2). The surface area of T45 is calculated to be 95 m^2/g, while for T65 and T85 samples, the surface area corresponds to 25 and 4 m^2/g, respectively, The lowering in the surface area may be due to the increase in the grain size and particle growth during high-temperature annealing.

Optical study

Diffuse reflectance spectroscopy was carried out to analyze the optical spectral response of all the samples. Figure 5 shows the absorbance curve. The absorption band around 370 nm can be assigned to the band gap excitation of anatase TiO_2 that corresponds to the band to band transition from Ti 3d level to O 2p levels (Devi et al. 2010).

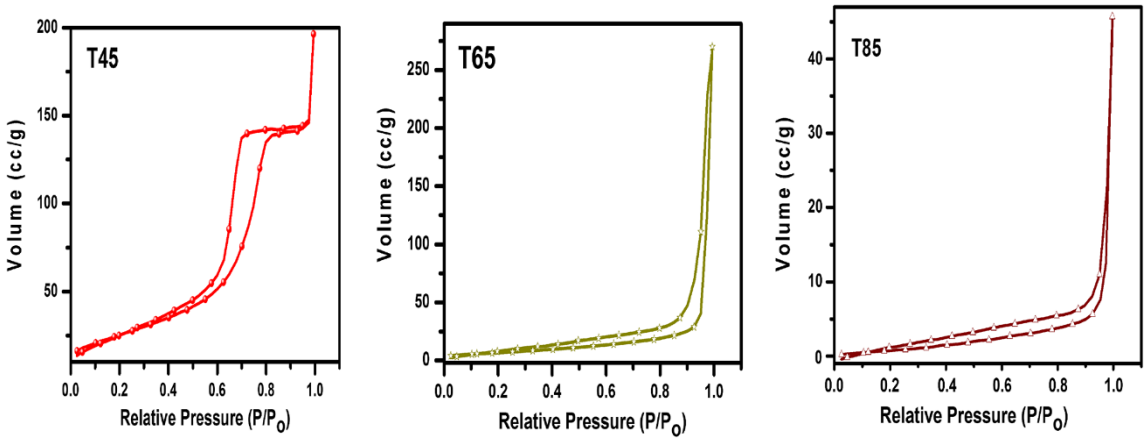

Fig. 4 Isotherm curve of all the samples

Table 2 Surface area and pore size distribution of all the samples

SI. no.	Sample	Surface area (m^2/g)	Pore size (nm)
1.	T45	95	31
2.	T65	25	5
3.	T85	4	3

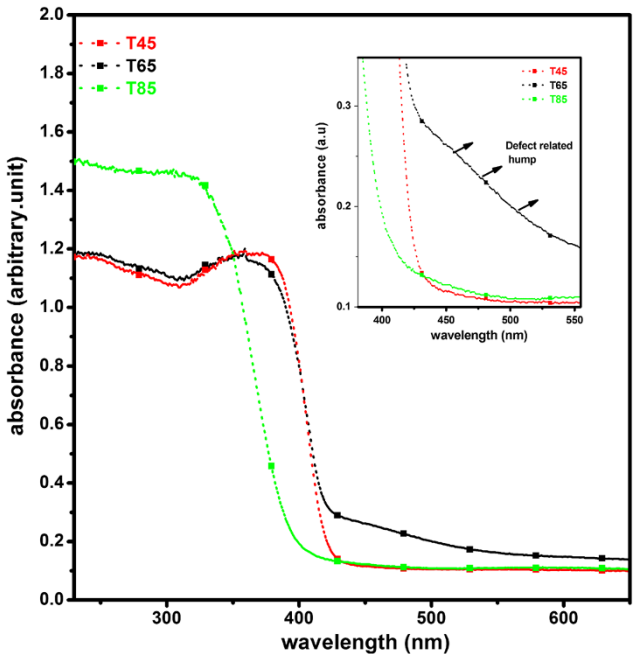

Fig. 5 UV–Vis absorption study annealed at different temperatures

Compared to T45, the absorption spectra of the mixed phase sample, T65 shows a hump in the visible region (420–540 nm) (inset, Fig. 5) due to the defects present at the anatase–rutile contacts. In T85 sample, an enhancement in the absorption is noticed and this is possibly due to the presence of rutile content that has smaller band gap in comparison to pristine anatase phase (Zhang et al. 2010).

TiO_2 is an indirect band gap material and the band gap is evaluated by drawing a line on the linear part of the curve, $[F(R)hv]^{1/2}$ vs hv at $[F(R)hv]^{1/2} = 0$. Band gap values of each sample are shown in Fig. 6. The band gap of T45 is slightly higher than that of bulk anatase and this is due to quantum confinement effect. The band gap of T85 matches with the band gap of bulk rutile TiO_2, while T65 has a band gap lower than that of either anatase (3.2 eV) or rutile (3.0 eV) TiO_2. This lowering in the band gap in T65 is due to the presence of defect bands that perturb the band structure by forming additional states within the band gap in the form of tails. This tail is referred to as the Urbach tail and the associated energy as the Urbach energy, expressed by the formula (Lethy et al. 2008):

$$\alpha = \alpha_o \exp \frac{E}{E_u} \tag{7}$$

α is the absorption co-efficient, E the photon energy and E_u is the Urbach energy. For the calculation of Urbach energy, we have plotted ln A (or ln $F(R)$ in DRS mode) vs E (eV) (Fig. 7). The reciprocal of the slopes of the linear portion below the optical band gap gives the Urbach energy. Table 1 gives the band gap and the corresponding Urbach energy of all the samples. The Urbach energy is calculated to be maximum for T65. In the TiO_2 nanoparticles, Ti^{4+} is surrounded by six oxygen ions forming the TiO_6^{2-} octahedra. High-temperature annealing at 650 °C alters the arrangement of oxygen ions around Ti^{4+} and generates a considerable amount of oxygen vacancies due to breaking of the Ti–O bond. In T65 the anatase and rutile phase being in contact with each other the defect by and large localizes at the contact of these two phases. These increase the width of the defect band and in turn increase the Urbach energy. In T85, a decrease in oxygen defect density decays the Urbach tail and increases the band gap (Zhang et al. 2008).

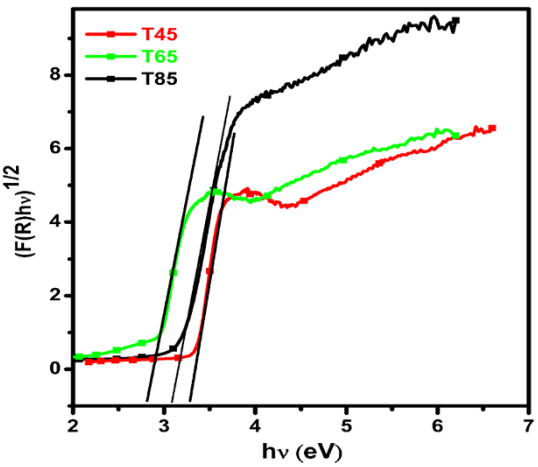

Fig. 6 Kubelka–Munk plot showing the variation in band gap

Photoluminescence is a very versatile and commonly used tool to disclose the efficiency of charge carrier trapping, immigration and transfer in semiconductors. Figure 8 exhibits the PL spectra of the samples at an excitation wavelength of 320 nm (3.87 eV). T45 has a UV emission at 392 nm and is the band edge emission of host TiO_2 arising from X_{1b} transition to Γ_3 (Serpone et al. 1995). In addition, there appear two blue emission peaks at 457 (2.7 eV) and 490 nm (2.5 eV) and one green emission peak at 537 nm (2.37 eV). The peak at 425 nm (2.9 eV) is probably due to the self-trapped exciton on the TiO_6 octahedra (Knorr Fritz et al. 2008; Wan et al. 2010). However, the same peak in rutile TiO_2 is due to recombination of free excitons (Yamada and Kanemitsu 2010). The blue emission peak at 490 nm is due to the charge transfer transition from Ti^{3+} to oxygen anion in a TiO_6^{2-} complex associated with oxygen vacancies (Yu et al. 2002). Another blue emission peak at 457 nm and green emission peak at 537 nm are due to the color centers associated with oxygen vacancies (Nick 2006).

The PL emission intensity is contributed by both radiative and non-radiative centers. Radiative recombination increases the emission intensity, while non-radiative recombination decreases the intensity. In our study, the emission intensity of T65 decreases as compared to the T45 sample. The decrease in intensity is due to the presence of defects that act as non-radiative centers. Another reason may be due to the trap to trap relocation of electron until a recombination center is anticipated. The process restrains the electron–hole recombination and quenches the emission intensity. In T85 sample, high-temperature annealing removes some of the defects and so the emission intensity increases inferring increase in charge carrier recombination rate compared to T65 sample (Jung and Kim 2009).

To better understand the recombination process, we have studied the PL decay curve (Fig. 9). The curves have been fitted with tri-exponential decay response functions defined by the following equation:

$$Y = y_0 + A_1 \times \exp\left(-(x - x_0)/t_1\right) + A_2 \times \exp\left(-(x - x_0)/t_2\right) + A_3 \times \exp\left(-(x - x_0)/t_3\right) \quad (8)$$

where y_0 is the baseline correction, t_1, t_2, t_3 the decay constants and A_1, A_2, A_3 are the pre-exponential factors. The average decay $< \tau_{avg} >$ time is calculated using the following formula (Das et al. 2009):

$$< \tau_{avg} > = \frac{\sum_{i=1}^{i=3} A_i t_i^2}{\sum_{i=1}^{i=3} A_i t_i} \quad (9)$$

Using the above equation, the average lifetime for T45, T65, T85 are calculated to be 1.99, 2.13 and 1.65 ns, respectively. T65 has a longer lifetime compared to T45 and T95. The charge carrier lifetime is affected by several

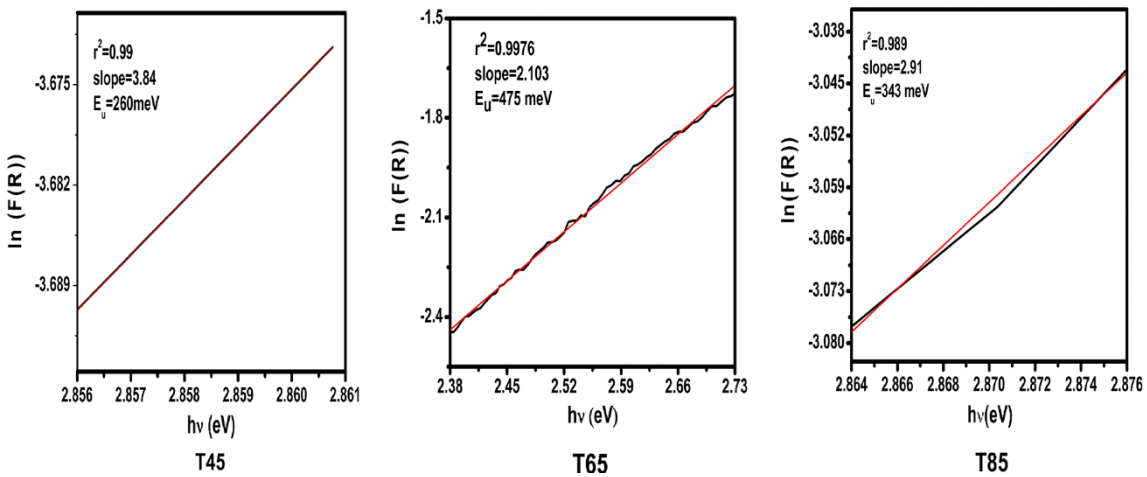

Fig. 7 Urbach energy plots for all the samples

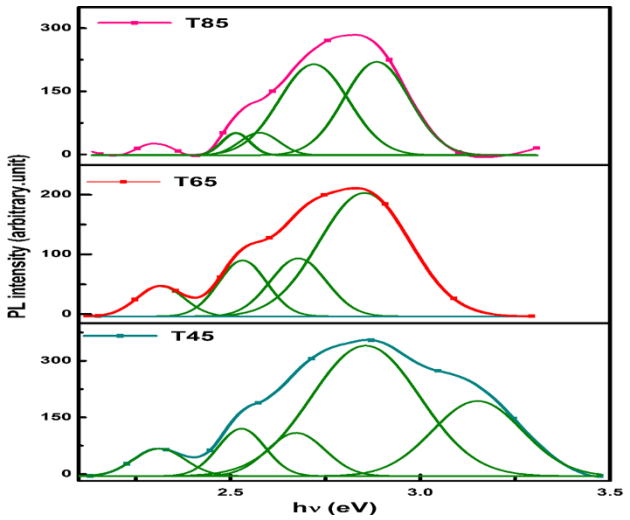

Fig. 8 Room-temperature photoluminescence after excitation at 320 nm

factors such as band structure, carrier trapping, mobility of the carriers, etc. Anatase TiO_2 being an indirect semiconductor, the conduction band electron and the valence band holes are in different positions in the Brillouin zone (Yamada and Kanemitsu 2012). The extent of overlapping of the wave function is therefore low. Inclusion of defects within the band gap further lowers the strength of overlapping and increases the lifetime of the charge carriers. Baiju et al. (2009) stated that the charge carriers have a longer lifetime when the anatase and rutile phases are in intimate contact. In case of T85, decrease in lifetime is due to increased recombination process (Jung and Kim 2009).

Thus, in the present investigation, the presence of peaks in the visible region, maximum quenching in emission intensity and increased lifetime for T65 samples throw light on the feasibility of the sample to act as a good photocatalytic candidate.

Photocatalytic activity

The photocatalytic activity of the samples is evaluated by analyzing the degradation of phenol under visible light. In the photocatalysis process, after light absorption by host TiO_2, electrons and holes so formed combine with water or OH group, and water-dissolved oxygen get adsorbed on different active sites of the photocatalyst to form the hydroxyl radical and the super oxide anion. These hydroxyl radical and super oxide anion act as the potential agents in the photocatalytic degradation process.

$$TiO_2 \longrightarrow hve^- + h^+$$

$$OH^{\cdot} + h^+ \longrightarrow hvOH^{\cdot}$$

$$O_{2+}e^- \longrightarrow hvO_2^-$$

$$\text{Phenol} + {}^{\cdot}O_2^- \rightarrow \text{Products}$$

$$\text{Phenol} + OH^{\cdot} \rightarrow \text{Products}$$

Figure 10 shows the photocatalytic degradation curve. From the graph, T65 is found to exhibit better degradation compared to T45 and T85. Under Visible light irradiation, the photogenerated electrons rapidly transfer from rutile to lower energy anatase trapping site (Fig. 11). This leads to a more stable charge separation and in turn contributes to increased photocatalytic activity (Hurum et al. 2003).

It is worth mentioning that although the surface area and pore size in T65 are lower than T45, such high photocatalytic activity is attributed to the intimate anatase–rutile contacts that generates considerable amount of defects. These defects promote the charge separation and restrain the electron–hole recombination which in turn increases the lifetime of the photoinduced charge carriers as seen from the luminescence decay curve. The generated charge carriers interact with the phenol before they recombine and hence results in higher degradation activity.

In T85, high-temperature annealing removes most of the defects and thereby increases the carrier mobility. The

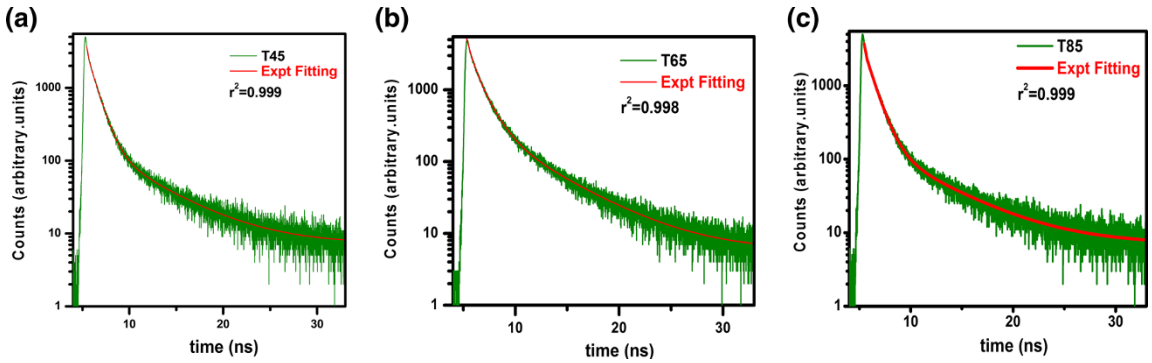

Fig. 9 Luminescence decay study

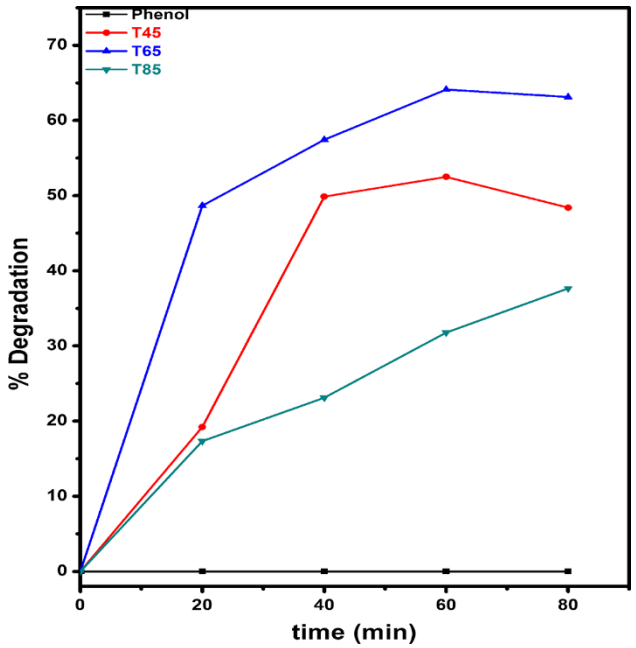

Fig. 10 Degradation curve of phenol under visible light illumination

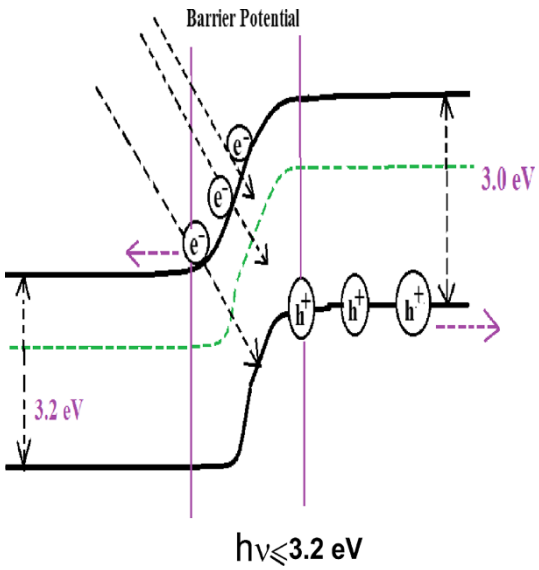

Fig. 11 Energy band profile with $h\nu < 3.2$ eV

increased carrier mobility induces the increased recombination process and hence lowers the photocatalytic activity (Jung and Kim 2009).

Conclusion

In summary, mixed phase nanocrystalline titania have been prepared employing a simple wet-chemical techniques. Thermal treatment of anatase-type titania precursor leads to transformation of anatase to rutile at 650 °C. In the photodegradation experiment, mixed phase titania (T65) are found to exhibit improved photocatalytic activity compared to pure anatase and pure rutile phase. Such enhancement in the photocatalytic activity is attributed to the formation of defects at the anatase–rutile interface. The presence of these defects lowers the band gap and increases the charge separation, thereby favoring two important criteria for an efficient photocatalytic process.

Acknowledgments We are thankful to Department Of Chemistry, IIT Mumbai for helping us in carrying out the TRPL measurement, Sophisticated Analytical Instrument Facility (SAIF), NEHU, Shillong for helping us in providing the HRTEM images. We are also thankful to University Grants Comission (UGC) and Department Of Science and Technology (DST) for financial support to the project F.No.42-785/2013 (SR) and SR/NM/NS-98/2010(G), respectively.

References

Aita CR (2007) Raman scattering by thin film nanomosaic rutile TiO_2 Appl. Phys Lett 90:213112–213115

Baalousha M, Nam YJ, Cole PA, Gaiser B, Fernandes TF, Hriljac JA, Jepson MA, Stone V, Tyler CR, Lead JR (2012) Characterisation of cerium oxide nanoparticles: Part 1 size measurements Environmental toxicology and chemistry. Environ Toxicol 31:983–993

Baiju KV, Zachariah A, Shukla S, Biju S, Reddy MLP, Warrier KGK (2009) Correlating photoluminescence and photocatalytic activity of mixed-phase nanocrystalline titania. Catal Lett 130: 130–136

Brojčin MG, Šćepanović MJ, Dohčević-Mitrović ZD, Hinić I, Matović B, Stanišić G, Popović ZV (2005) Infrared study of laser synthesized anatase TiO2 nanoparticles. J Phys D Appl Phys 38:1415–1420

Choudhury B, Borah B, Choudhury A (2011) Extending visible light photocatalytic activity of TiO_2 nanoparticles to visible region of illumination by doping of cerium. Photochem Photobiol 88:257–264

Das K, Sharma SN, Kumar M, De SK (2009) Morphology dependent luminescence properties of co doped TiO2 nanostructures. J Phys Chem C 113:14783–14792

Devi LG, Kottam N, Murthy BN, Kumar SG (2010) Enhanced photocatalytic activity of transition metal ions $Mn^{2+,}$ Ni^{2+}, Zn^{2+} doped polycrystalline titania for the degradation of aniline blue under UV/solar light'. J Mol Catal A: Chem 328:44–52

Dutta N, Mohanta D, Sulania I, Choudhury A (2009) Studies of optical properties and SHI irradiation on PbS sensitized nanoporous TiO_2 network. J Opt 38:169–176

Fujishima A, Honda K (1972) Electrochemical photolysis of water at a semiconductor. Nature 238:37–38

Georgescu D, Baia L, Ersen O, Baia M, Simon S (2012) Experimental assessment of the phonon confinement in TiO2 anatase nanocrystallites by Raman spectroscopy. J Raman Spect 43:876–883

Gupta SM, Tripathi M (2011) A review on TiO_2 nanoparticles. Chin Sci Bull 56:1639–1657

Hurum DC, Agrios AG, Gray KA, Rajh T, Thurnauer C (2003) Explaining the enhanced photocatalytic activity of degussa P25 mixed-phase TiO_2 using EPR. J Phys Chem B 107:4545–4549

Jung HS, Kim H (2009) Origin of low photocatalytic activity of rutile TiO_2. Electron Mater Lett 5:73–76

Knorr Fritz J, Mercado Candy C, McHale Jeanne L (2008) Trap-state distributions and carrier transport in pure and mixed-TiO_2: influence of contacting solvent and interphasial electron transfer. J Phys Chem C 112:12786–12794

Lethy KJ, Beena D, Mahadevan Pillai VP, Ganesan V (2008) Bandgap renormalization in titania modified nanostructured tungsten oxide thin films prepared by pulsed laser deposition technique for solar cell applications. J Appl Phys 104:033515 (12 pp)

Li GH, Dimitrijevic NM, Chen L, Nichols JM, Rajh T, Gray KA (2008) The important role of tetrahedral Ti^{4+} sites in the phase transformation and photocatalytic activity of TiO_2 nanocomposites. J Am Chem Soc 130:5402–5403

Lin Y-C (2013) Applying Ag–TiO_2/functional filter for abating odor exhausted from semiconductor and opti-electronic industries. Clean Technol Environ Policy 15:359–366

Mali SM, Betty CA, Bhosale PN, Patil PS (2011) Hydrothermal synthesis of rutile TiO_2 with hierarchical microspheres and their characterization. Cryst Eng Commun 13:6349–6351

Marinel S, Choi DH, Heuguet R, Agarwal D, Lanagan M (2013) Broadband dielectric characterization of TiO_2 ceramics sintered through microwave and conventional processes. Ceram Int 39:299–306

Mazza T, Barborini E, Piseri P, Milani P, Cattaneo D, Bassi AL, Bottani CE, Ducati C (2007) Raman spectroscopy characterization of rutile TiO_2 nanocrystals. Phys Rev 75:045416 (5 pp)

Mo S, Ching WY (1995) Electronic and optical properties of three phases of titanium dioxide: rutile, anatase and brookite. Phys Rev B 51:13023–13032

Narksitipan S, Thongtem S (2012) Preparation and characterisation of rutile TiO2 films. J Ceram Process 13:35–37

Nick S (2006) Is the band gap of pristine TiO2 narrowed by anion- and cation-doping of titanium dioxide in second-generation photocatalysts. J. Phys Chem B 110:24287–24293

Orazen Erin L (2007) Raman spectroscopy on the nanoscale: an investigation of silver triangle arrays, polymer laminates and gold-loaded mesoporous titania fims. Dissertation, University Of California

Orendorz A, Brodyanski A, Losch J, Bai LH, Chen ZH, Le YK, Ziegler C, Gnaser H (2007) Phase transformation and particle growth in nanocrystalline anatase TiO2 films analyzed by X-ray diffraction and Raman spectroscopy. Surf Sci 601:4390–4394

Oye G, Glomn WR, Vralstad T, Volden S, Magnusson H, Stocker M, Sjoblom J (2006) Synthesis, functionalisation and characterisation of mesoporous materials and sol–gel glasses for applications in catalysis, adsorption and photonics. Adv Colloid Interface Sci 123–126:17–32

Paul S, Choudhury A, Bojja S (2013) Effect of nickel doping on the optical property and photocatalytic activity of titanium dioxide nanoparticles. Micro Nano Lett 8:184–187

Qui J, Zhang S, Zhao H (2011) Recent applications of TiO_2 nanomaterials in chemical sensing in aqueous media Sens. Actuat B: Chem 160:875–890

Serpone N, Lawless D, Khairutdinov R (1995) Size effects on the photophysical properties of colloidal anatase TiO2 particles: size quantization versus direct transitions in this indirect semiconductor. J Phys Chem 99:16646–16654

Sharma S, Chaudhary S, Kashyap SC, Malik VK (2011) DC magnetization investigations in $Ti_{1-x}Mn_XO_2$ nanocrystalline powder. J Alloy Compd 509:7434–7438

Shin K, J-B Yoo, Park JH (2013) Photoelectrochemical cell/dye-sensitized solar cell tandem water splitting systems with transparent and vertically aligned quantum dot sensitized TiO2 nanorod arrays. J Power Sour 225:263–268

So WW, Park SB, Kim KJ, Shin CH, Moon SJ (2001) The crystalline phase stability of titania particles prepared at room temperature by the sol–gel method. J Mater Sci 36:4299–4305

Song S, Liu Z, He Z, Zhang A (2010) Impacts of morphology and crystallite phases of titanium oxide on the catalytic oxidation of phenol. Environ Sci Technol 44:3913–3918

Spurr RA, Myers H (1957) Quantitative analysis of anatase-rutile mixtures with an X-ray diffractometer. Anal Chem 29:760–762

Volkan M, Stokes DL, Vo-Dinh T (2005) A sol–gel derived AgCl photochromic coating on glass for SERS chemical sensor application. Sens Actuat B: Chem. 106:660–667

Wan YW, Chang YM, Ting JM (2010) Room-temperature synthesis of single-crystalline anatase TiO_2 nanowires. Cryst Growth Des 10:1646–1651

Wang D, Zhao J, Chen B, Zhu C (2008) Lattice vibration fundamentals in nanocrystalline Anatase investigated with Raman scattering. J Phys: Condens Matter 20:085212 (7 pp)

Yamada Y, Kanemitsu Y (2010) Blue photoluminescence of highly photoexcited rutile TiO_2: nearly degenerate conduction-band effects. Phys Rev B 82:113103 (4 pp)

Yamada Y, Kanemitsu Y (2012) Determination of electron and hole lifetimes of rutile and anatase TiO_2 single crystals. Appl Phys Lett 101:133907

Yu JC, Yu J, Ho W, Jiang Z, Zhang L (2002) Effects of F^- doping on the photocatalytic activity and microstructures of nanocrystalline TiO_2 powders. Chem Mater 14:3808–3816

Zhang WF, He YL, Zhang MS, Yin Z, Chen Q (2000) Raman scattering on anatase TiO_2 nanocrystals. J Phys D: Appl Phys 33:912–916

Zhang H, Xie C, Zhang Y, Liu G, Li Z, Liu C, Ma X, Zhang W (2008) Effects of thermal treatment under different atmospheres on the spectroscopic properties of nanocrystalline TiO_2. J Appl 103:103107 (4 pp)

Zhang Y, Chen J, Li X (2010) Preparation and photocatalytic performance of anatase/rutile mixed-phase TiO_2 nanotubes. Catal Let 139:129–133

Zhou J, Zhang Y, Zhao XS, Ray AK (2006) Photodegradation of benzoic acid over metal-doped TiO_2. Ind Eng Chem Res 45:3503–3511